## PAPER

# Narrow-bandgap Sn–Pb mixed perovskite single crystals for high-performance near-infrared photodetectors†

Zhizhen Chang,‡[a] Zhengjun Lu,‡[a] Wei Deng, [ID] *[a] Yandi Shi,[a] Yuye Sun,[a] Xiujuan Zhang [ID] *[a] and Jiansheng Jie [ID] *[a,b]

Narrow-bandgap Sn–Pb mixed perovskite single crystals are highly promising as photoactive materials for efficient and low-cost near-infrared (NIR) photodetectors. However, because of the significant difference in the crystallization velocities for Pb- and Sn-based perovskites, Sn–Pb mixed perovskites are peculiarly prone to phase separation during the crystallization process, causing the degradation of the optical and electronic properties of materials. Herein, we propose a low-temperature space-confined technique (LT-SCT) that simultaneously reduces the crystallization velocities of pure Sn and Pb perovskites, enabling the fabrication of pure-phase $(FASnI_3)_{0.1}(MAPbI_3)_{0.9}$ single crystals. The resulting $(FASnI_3)_{0.1}(MAPbI_3)_{0.9}$ single crystals exhibit excellent crystallinity with a high hole mobility of $7.44 \times 10^3$ cm$^2$ V$^{-1}$ s$^{-1}$ and a low surface trap density of $1.88 \times 10^9$ cm$^{-2}$. These properties benefit the application of $(FASnI_3)_{0.1}(MAPbI_3)_{0.9}$ single crystals in self-powered NIR photodetectors and yield outstanding comprehensive performance, especially with a broad linear dynamic range of up to 163.5 dB, a large responsivity ($R$) of 0.53 A W$^{-1}$, and a fast response speed of 22.78 µs in the NIR spectral region (750–860 nm). Furthermore, high-quality NIR imaging and wearable health monitoring are achieved by employing high-performance and self-driven NIR photodetectors. This work contributes to developing Sn–Pb mixed perovskite single crystals and provides a promising candidate for efficient and low-cost NIR photodetection.

## Introduction

Near-infrared (NIR) photodetectors, which have spectral responses from 750 to 1400 nm, have received much attention due to their tremendous potential applications, including biometric authentication, health monitoring, machine vision, biomedical imaging and so on.[1–4] State-of-the-art commercial NIR photodetectors are dominated by single-crystalline inorganic materials like silicon (Si),[5] germanium (Ge),[6] and III–V compound indium gallium arsenide (GaInAs),[7] but their use is curbed by high-cost and complicated manufacturing procedures, thus limiting their appealing deployment in large-scale optoelectronic applications.[8] On the other hand, they are

inherently rigid and fragile; this feature fundamentally determines that inorganic NIR photodetectors have limitations for application in emerging flexible and wearable technology.[9] Therefore, development of intrinsically flexible narrow-bandgap semiconducting materials such as organic materials,[10–12] quantum dots,[13] and perovskites[14] for NIR photodetectors is urgently needed.[15–17]

Recently, emerging Sn–Pb mixed perovskites have presented enormous potential as narrow-bandgap photoactive materials of NIR photodetectors.[18–23] They not only can be easily produced as large-area crystalline films by simple low-temperature solution-processing methods but also possess exceptional optoelectronic properties in terms of tunable band gaps, high charge carrier mobility, and large absorption coefficients that are over one order of magnitude greater than those of Si.[14,24] The first Sn–Pb mixed perovskite-based NIR photodetector was proposed by Jen *et al.* in 2017,[19] and an incipient photoresponsivity of ~0.35 A W$^{-1}$ was obtained at 800 nm. After five years of unremitting endeavors, remarkable achievements have been made in finely regulating compositions, suppressing Sn$^{2+}$ oxidation, and invoking new deposition methods, resulting in a relatively high NIR photoresponse and stability for Sn–Pb perovskite-based devices.[14,22,23] To date, most of the

[a]Institute of Functional Nano & Soft Materials (FUNSOM), Jiangsu Key Laboratory for Carbon-Based Functional Materials & Devices, Soochow University, Suzhou, Jiangsu 215123, P. R. China. E-mail: dengwei@suda.edu.cn, xjzhang@suda.edu.cn, jsjie@suda.edu.cn
[b]Macao Institute of Materials Science and Engineering, Macau University of Science and Technology, Taipa, Macau SAR 999078, P. R. China
†Electronic supplementary information (ESI) available. See DOI: https://doi.org/10.1039/d2nr05800f
‡These authors contributed equally to this work.

Sn-containing perovskite NIR photodetectors have been often limited by polycrystalline photoactive layers, as reflected by their low photodetection efficiency, large noise current, and fast performance degradation in an ambient environment. As expected, Sn–Pb perovskite single crystals with an absence of grain boundaries and an extremely low trap density will show superior physical properties and have much better performance than their polycrystalline counterparts.[25,26] However, until now, compared with widespread pure Pb perovskite single crystals, Sn–Pb mixed perovskite single crystals have not been reported yet. One of the main reasons is the substantial difference between the crystallization rates of Pb- and Sn-based perovskites.[27] In general, Sn-containing perovskites have a faster crystallization rate and this scenario arouses phase separation, forming single-component Pb and Sn perovskites.[28] The existing phase separation negatively affects the light absorption properties and charge carrier transport, deteriorating the NIR photodetection efficiency.

In this work, we, for the first time, report the fabrication of narrow-bandgap Sn–Pb mixed perovskite single crystals by a low-temperature space-confined technique (LT-SCT) and demonstrate a perovskite single-crystal NIR photodetector. By confining the Sn–Pb perovskite precursors into a micrometer-sized gap at room temperature, the crystallization velocities of Pb and Sn perovskites are significantly reduced simultaneously, enabling us to obtain pure-phase $(FASnI_3)_{0.1}(MAPbI_3)_{0.9}$ single crystals. The as-fabricated $(FASnI_3)_{0.1}(MAPbI_3)_{0.9}$ single crystals show a remarkably high mobility of $7.44 \times 10^3$ cm$^2$ V$^{-1}$ s$^{-1}$ and a low surface trap density of $1.88 \times 10^9$ cm$^{-2}$, and high absorption in the NIR region; these two values are superior to those of reported Sn–Pb mixed polycrystalline films. The high-quality $(FASnI_3)_{0.1}(MAPbI_3)_{0.9}$ single crystals contribute to reducing the dark current and enhancing the photocurrent of devices. Ultimately, we achieved a self-powered photodetector with outstanding comprehensive performance in terms of a high external quantum efficiency (EQE) of 82.5%, large responsivity ($R$) of 0.53 A W$^{-1}$, high specific detectivity ($D^*$) of $7.09 \times 10^{10}$ Jones, broad linear dynamic range (LDR) of up to 163.5 dB, and fast response speed in the NIR spectral region (750–860 nm). The efficient, self-driven NIR photodetector allowed us to demonstrate its great potential for application in wearable health monitoring and imaging. This work paves the way toward cost-effective and high-performance NIR photodetectors.

## Experimental section

### Materials

MAI (methanaminium iodide, ≥99.5%), PbI$_2$ (lead iodide, >99.99%), poly(bis(4-phenyl) (2,4,6-trimethylphenyl) amine (PTAA, $M_n$ = 15 000–25 000), and 2,9-dimethyl-4,7-diphenyl-1,10-phenanthroline (BCP, >99%) were purchased from Xi'an Polymer Light Technology Corp. FAI (formamidinium, 99.5%) was purchased from Dyesol. SnI$_2$ (tin iodide, 99.99%), SnF$_2$

(tin(II) fluoride, 99%), and Pb(SCN)$_2$ (lead thiocyanate, 99.5%) were purchased from Sigma-Aldrich. C$_{60}$ ([60] fullerene, >99.5%) was purchased from Luminescence Technology Corporation. PCBM ([6,6]-phenylC$_{61}$-butyric acid methyl ester, 99.9%) was purchased from Solenne BV. γ-Butyrolactone (GBL, 99%) and trichloro (1$H$,1$H$,2$H$,2$H$-perfluorooctyl) silane (FTS, 97%) were purchased from J&K Scientific. Propylene carbonate (PC, 99.7%) was purchased from Sigma-Aldrich. Toluene (99.8%) and chlorobenzene (99.9%) were purchased from Alfa Aesar. All materials were used as received without any further purification.

### Preparation of perovskite precursor solution and substrates

The FASnI$_3$ precursor solution was prepared by dissolving 59.5 mg of SnI$_2$ and 33.0 mg of FAI with 10 mol% (2.5 mg) of SnF$_2$ in 200 μL PC/GBL (65% : 35% v/v). The MAPbI$_3$ precursor solution was prepared by dissolving 157.7 mg PbI$_2$ and 65.3 mg MAI with 3.5 mol% (3.866 mg) of Pb(SCN)$_2$ in 300 μL PC/GBL (65 : 35, v/v). These precursor solutions were stirred overnight at 37 °C in a nitrogen-filled glovebox. The $(FASnI_3)_{0.1}(MAPbI_3)_{0.9}$ precursor solution was obtained by mixing FASnI$_3$ and MAPbI$_3$ precursor solutions in a stoichiometric ratio of 1 : 9 and stirred for 1 h at 37 °C in a nitrogen-filled glovebox. The indium tin oxide (ITO) substrates and glass substrates were sonicated in acetone, DI (deionized) water, and ethanol sequentially. Next, PTAA solution (0.2 wt% in toluene) was spin-coated on the ITO substrate for 30 s at 4000 rpm and subsequently annealed at 100 °C for 10 min. The glass substrate coated with hydrophobic FTS molecules was obtained by placing the glass substrate under an FTS vapour atmosphere at 90 °C for 15 min.

### Growth and characterization of $(FASnI_3)_{0.1}(MAPbI_3)_{0.9}$ single crystals

A 5 μL volume of $(FASnI_3)_{0.1}(MAPbI_3)_{0.9}$ solution was dropped on the PTAA/ITO substrate preheated to the solution temperature and enclosed by an FTS-coated glass substrate. Subsequently, the two substrates, clamped together *via* a clip, were then placed on a hotplate at a temperature of 25–30 °C to induce nucleation and growth. The gap between the upper and lower substrates is controlled by adjusting the applied force of the clip to optimize the thickness of the crystal. Finally, the two substrates were separated to obtain thin single crystals on the PTAA/ITO substrate, which was then slowly cooled to room temperature on the hotplate for further solvent removal. All the experiments were carried out in a nitrogen-filled glovebox. The morphological and crystal thickness characterization of $(FASnI_3)_{0.1}(MAPbI_3)_{0.9}$ single crystals was performed using an optical microscope (Olympus, BX51), a 3D optical surface metrology system (Leica, DCM8), a scanning electron microscope (SEM, Carl Zeiss, Supra55 and G500) with an accelerating voltage of 8 kV, and an atomic force microscope (AFM, Oxford, Asylum Cypher S). A transmission electron microscope (TEM, FEI, Tecnai G2 F20) was used to characterize the crystal structure of the $(FASnI_3)_{0.1}(MAPbI_3)_{0.9}$ single crystals. An X-ray diffractometer (Bruker, D8. Discover) was used to investigate

the large-area crystallinity of the $(FASnI_3)_{0.1}(MAPbI_3)_{0.9}$ single crystals. The optical properties of the $(FASnI_3)_{0.1}(MAPbI_3)_{0.9}$ single crystals were measured using a UV-VIS-NIR spectrophotometer (PerkinElmer, Lambda 950 model) and a fluorescence spectrometer (Hitachi, F-4600).

### Device fabrication and measurement

Vertical-type photodiode fabrication was completed by depositing the electron transport layer and the electrode on the preprepared $(FASnI_3)_{0.1}(MAPbI_3)_{0.9}$ single crystal in sequence. To fabricate the device, one high-quality single crystal was used; the yield of workable crystals was approximately 70%. A 2 wt% $PC_{61}BM$ solution in chlorobenzene was spun on the perovskite layer at 1000 rpm in a nitrogen-filled glovebox and then annealed at 100 °C for 15 min. After that, a metal shadow mask was placed in alignment with the perovskite layer and the patterned ITO/glass film through a home-built mask alignment system. Then, $C_{60}$ (20 nm), BCP (3 nm), and Ag (silver, 80 nm) layers were thermally evaporated successively through the shadow mask. The effective area of each device was 72 × 96 μm². The current ($I$)–voltage ($V$) measurements of the vertical-type photodiode were performed utilizing a semiconductor characterization system (Keithley, S4200) and a micromanipulator probe station (Cascade M150). The light illumination on the device was generated using an 808 nm LED and a laser (FC-808-3000-MM), which was further calibrated with a silicon photodiode (Newport, model 843-R). All the sample preparation processes and characterization studies were conducted in air. The shadow mask contains 58 hollowed-out squares (1 cm × 1 cm), forming an imaging target "cat" pattern. The spot size of the 808 nm laser was 0.196 cm², which could completely illuminate the device (size of 72 × 96 μm²). Before testing, the laser was aligned with the detector and the shadow mask was placed between them. The photodetector scanned the imaging target in two dimensions and the photocurrent was recorded during scanning. After that, the output current values were used to reconstruct the target image.

### Flexible device fabrication

For flexible device fabrication, rigid substrates were changed to ITO-coated polyethylene terephthalate (PET). The flexible substrates were sonicated for 15 min in acetone, DI water, and ethanol sequentially. Next, the cleaned ITO/PET was irradiated by ultraviolet (UV) light for 15 min. A PTAA solution was spin-coated on the ITO/PET substrate for 30 s at 4000 rpm and subsequently annealed at 100 °C for 10 min. Subsequently, the $(FASnI_3)_{0.1}(MAPbI_3)_{0.9}$ single crystals were grown on the prepared PTAA/ITO/PET substrates. The conditions for crystal growth on flexible substrates were the same as those on rigid substrates. All the experiments were carried out in a nitrogen-filled glovebox. The flexible device was completed by depositing the electron transport layer and the electrode on the preprepared $(FASnI_3)_{0.1}(MAPbI_3)_{0.9}$ single crystal on PTAA/ITO/PET in sequence. The flexible device fabrication details of the deposition of the ETL and electrode were the same as those of the rigid device.

## Results and discussion

The early reported Sn–Pb perovskites consist of MA components, but MA is thermally unstable and easy to chemically decompose.[29] Therefore, we partially substituted MA with FA, which has been proved to improve stability in previous reports,[30,31] and used $(FASnI_3)_{0.1}(MAPbI_3)_{0.9}$ as the Sn–Pb perovskite. Given the phenomenon of phase separation in Sn–Pb mixed perovskites, we developed an LT-SCT to grow $(FASnI_3)_{0.1}(MAPbI_3)_{0.9}$ single crystals. Fig. 1a shows a schematic representation of the LT-SCT, in which a tiny amount of the $(FASnI_3)_{0.1}(MAPbI_3)_{0.9}$ perovskite precursor was dropped on a PTAA/ITO glass slide, and then the droplet was confined by an upper slide. The upper substrate was treated with FTS to realize a lyophobic surface with a larger solvent contact angle than the underlying substrate (Fig. 1b). The FTS modification details are described in Fig. S1, ESI.† This surface treatment ensures that the perovskite solute preferentially undergoes heterogeneous nucleation at the PTAA surface and could accelerate solute diffusion to maintain long-range in-plane crystallization growth in the narrow interspace.[25,32] Subsequently, the sample was placed into a nitrogen glovebox to control the slow evaporation of solvent at room temperature. After about four days, $(FASnI_3)_{0.1}(MAPbI_3)_{0.9}$ single crystals formed on the PTAA/ITO substrate. Fig. 1c shows a top-view optical microscopy photograph of a typical $(FASnI_3)_{0.1}(MAPbI_3)_{0.9}$ single crystal with a regular shape and a lateral dimension reaching 696 × 431 μm. A zoomed-in SEM image (Fig. 1d) clearly reveals the angled facet and smooth surface without grain boundaries and visible defects. Even in high-resolution SEM images, no grain structure was observed on the crystal, providing further evidence of its high quality (Fig. S2, ESI†). In contrast, the $(FASnI_3)_{0.1}(MAPbI_3)_{0.9}$ polycrystalline film was composed of a large number of "small" crystal domains that exhibited many grain boundaries with significant surface roughness (Fig. S3, ESI†). Using AFM to quantificationally compare $(FASnI_3)_{0.1}(MAPbI_3)_{0.9}$ single crystal (Fig. 1e) and polycrystalline film (Fig. S4, ESI†) surfaces revealed a distinctly different root mean square (RMS) roughness of 1.31 nm vs. 161.44 nm. Importantly, our LT-SCT could be universally applicable to various perovskites with different molar ratios of Sn to Pb, such as 1 : 4 and 3 : 7. All the Sn–Pb mixed perovskite single crystals presented flat surface morphologies and grain boundary-free structures, as seen in the SEM images (Fig. S5, ESI†). From 3D surface topographic measurements (Fig. 1f), we found that the approximate thickness of the $(FASnI_3)_{0.1}(MAPbI_3)_{0.9}$ single crystal was 1.4 μm; such a thick crystal is a prerequisite for a high NIR response since it can harvest nearly 95% of the incident NIR light, according to a previous report.[31]

A single crystal has a superior crystallinity and optoelectronic properties in comparison with polycrystalline films. Next, we confirmed these characteristics by inspecting the crystalline structure, and optical and transport properties of the $(FASnI_3)_{0.1}(MAPbI_3)_{0.9}$ single crystal. The X-ray diffraction (XRD) patterns of the $(FASnI_3)_{0.1}(MAPbI_3)_{0.9}$ single crystal
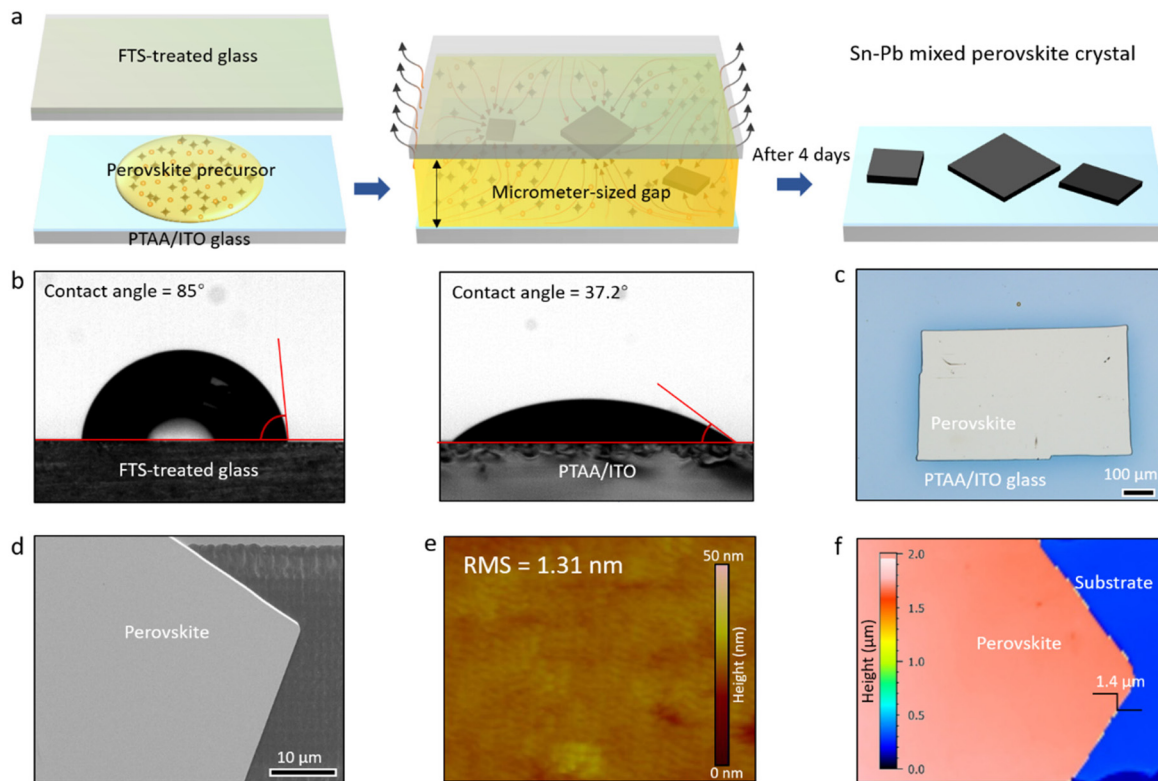
**Fig. 1** Fabrication of Sn–Pb mixed perovskite single crystals. (a) Schematic representation of the LT-SCT method for producing $(FASnI_3)_{0.1}(MAPbI_3)_{0.9}$ single crystals. (b) Contact angles of the perovskite precursor on the FTS-treated glass and PTAA surfaces. (c) Optical image of a representative $(FASnI_3)_{0.1}(MAPbI_3)_{0.9}$ single crystal. (d) Zoomed-in SEM, (e) surface topography and (f) 3D topography images of the $(FASnI_3)_{0.1}(MAPbI_3)_{0.9}$ single crystal.

shown in Fig. 2a reveal a typical tetragonal lattice with only two major diffraction peaks of the (200) and (400) planes, indicating that the out-of-plane orientation of the crystal is the (k00) plane. We further analysed the crystal quality through XRD rocking curve (XRC) analysis of the (200) diffraction. The full width at half-maximum was found to be 0.033° (Fig. 2b). The narrow width of the peak is much smaller than that of its polycrystalline film (Fig. S6, ESI†) and comparable to the other reported values for perovskite single crystals (Table S1, ESI†).[34–44] TEM was further used to characterize the $(FASnI_3)_{0.1}(MAPbI_3)_{0.9}$ single crystal that was directly grown on a Cu grid (Fig. 2c). The selected-area electron diffraction (SAED) pattern collected from the $(FASnI_3)_{0.1}(MAPbI_3)_{0.9}$ single crystal presented hexagonally symmetric spots with high brightness (Fig. 2c). The above results collectively verify the single-crystalline nature of our sample.
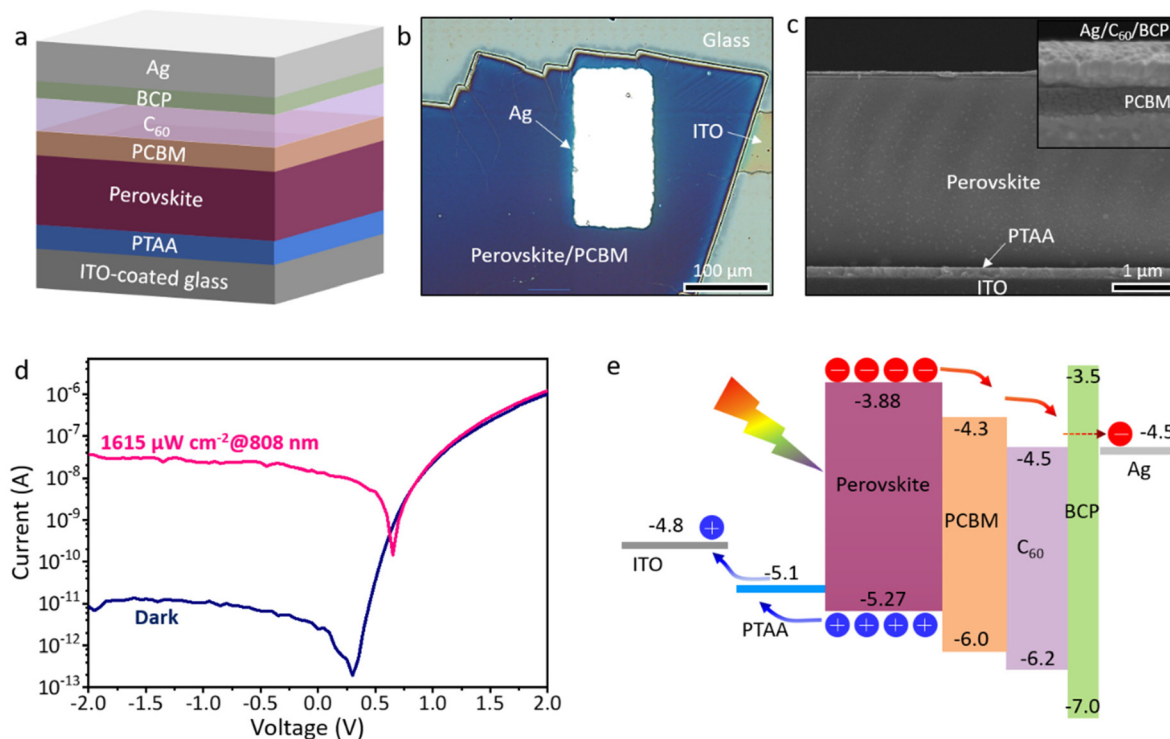
The absorption spectrum of the $(FASnI_3)_{0.1}(MAPbI_3)_{0.9}$ single crystal exhibits an extended absorption edge to (NIR) wavelengths compared with that of the pure lead perovskites.[25,26] The absorption onset is located at the wavelength of 920 nm (Fig. 2d), corresponding to a bandgap of 1.35 eV, as extracted from the Tauc plot of the absorption spectrum (Fig. 2e). We also observed that the PL peak at 860 nm is short of the absorption onset, indicating that PL emission can be extinguished by itself, as reported before.[26,32] The high-quality

crystal contributed significantly to the reduced surface trap density and improved carrier mobility. We evaluated these two values of the $(FASnI_3)_{0.1}(MAPbI_3)_{0.9}$ single crystal by space-charge-limited current (SCLC) measurements, as shown in Fig. 2f. A lateral device with a channel width and length of 180 and 300 μm, respectively, was fabricated using Au top electrodes. According to the Geurst theory,[33] we can calculate the surface trap density and carrier mobility of the as-grown $(FASnI_3)_{0.1}(MAPbI_3)_{0.9}$ single crystal from the I–V curve (the calculation details are discussed in the ESI†). The hole mobility and surface trap density were about $7.44 \times 10^3$ cm$^2$ V$^{-1}$ s$^{-1}$ and $1.88 \times 10^9$ cm$^{-2}$, respectively. These values are on a par with those of previously reported perovskite crystals.[25,26,32,33]

The high-quality and low-bandgap $(FASnI_3)_{0.1}(MAPbI_3)_{0.9}$ single crystal will show appealing potential in realizing NIR detection. In order to demonstrate this potential, we fabricated its photodetector with a multiple-layer architecture, as schematically shown in Fig. 3a. PTAA was spin-coated on the patterned ITO substrate as the hole transport layer (HTL). In addition, PTAA has a wetting characteristic to the perovskite solution, which can help to form large-sized crystals. A patterned ITO strip was selected as the bottom electrode because it can accurately define the device area. Subsequently, the $(FASnI_3)_{0.1}(MAPbI_3)_{0.9}$ single crystal was directly grown on PTAA. Then, PC$_{61}$BM (90 nm)/C$_{60}$ (20 nm) double fullerene
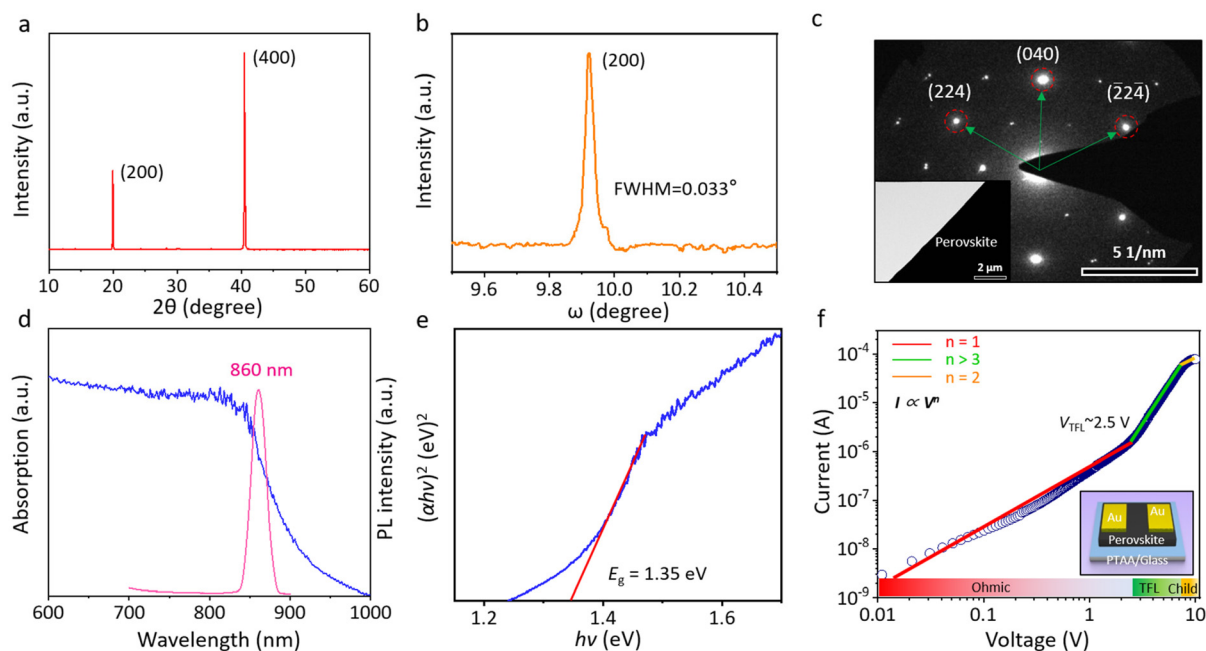
**Fig. 2** (a) XRD patterns of the $(FASnI_3)_{0.1}(MAPbI_3)_{0.9}$ single crystal. (b) High-resolution XRD rocking curve of the (200) diffraction. (c) TEM image of the as-grown $(FASnI_3)_{0.1}(MAPbI_3)_{0.9}$ single crystal and the corresponding SAED pattern. (d) Steady-state absorption and PL spectra of the $(FASnI_3)_{0.1}(MAPbI_3)_{0.9}$ single crystal. (e) Optical bandgap of the $(FASnI_3)_{0.1}(MAPbI_3)_{0.9}$ single crystal. (f) Scheme of the device structure for the SCLC method and current–voltage curve of the $(FASnI_3)_{0.1}(MAPbI_3)_{0.9}$ single crystal, which shows different regions marked with Ohmic, TFL, and Child, respectively.



**Fig. 3** (a) Schematic of a multiple-layer device architecture with the $(FASnI_3)_{0.1}(MAPbI_3)_{0.9}$ single crystal as the light absorption layer. (b) Optical image of the device. (c) Cross-sectional SEM image of the perovskite single-crystal device. (d) Current–voltage curves of the perovskite single-crystal NIR photodetector in the dark and under 808 nm light illumination (1615 μm $cm^{-2}$). (e) Band energy level alignment of the perovskite NIR photodetectors.

layers were coated onto the $(FASnI_3)_{0.1}(MAPbI_3)_{0.9}$ single crystal to function as the electron transport layer (ETL) due to their decent electron mobility and reduced resistance at the perovskite surface. Moreover, $PC_{61}BM$ also serves as an interlayer at the perovskite/ETL interface, which was confirmed to reduce the energy barrier and interfacial traps at the interface effectively.[45] Finally, a 3 nm BCP layer and 80 nm of Ag as the top electrode were deposited on the ETL using a shadow mask. Fig. 3b shows the top-view optical microscopy image of the $(FASnI_3)_{0.1}(MAPbI_3)_{0.9}$ single crystal-based device. It can be seen that the device area was determined to be the cross region of the top and bottom electrodes. A typical device area was about $6.9 \times 10^{-5}$ $cm^2$. The smooth and low defect $(FASnI_3)_{0.1}(MAPbI_3)_{0.9}$ single crystal could create an efficient charge carrier transport path and defect-free interface. The cross-sectional SEM image of the device (Fig. 3c) clearly certified this point, in which the $(FASnI_3)_{0.1}(MAPbI_3)_{0.9}$ single-crystal device featured a clean and flat interface. Fig. 3d shows the dark current and photocurrent curves (under 808 nm NIR light of 1615 μW $cm^{-2}$) of the $(FASnI_3)_{0.1}(MAPbI_3)_{0.9}$ single-crystal photodetector under a bias ranging from −2 to 2 V. It is seen that the $(FASnI_3)_{0.1}(MAPbI_3)_{0.9}$ single-crystal photodetector simultaneously achieves a low dark current and high photocurrent. Specifically, the device has a photocurrent of up to $1.32 \times 10^{-8}$ A under 0 V (photovoltaic mode). This implies efficient charge extraction and a large NIR response in the Sn–Pb perovskite single crystal. The high photocurrent also results from the strictly matched energy levels in the perovskite

heterojunction photodetector, as shown in Fig. 3e. Meanwhile, the dark current of our Sn–Pb perovskite single-crystal device is as low as 2.4 pA at 0 V. The low dark current should originate from the single-crystalline nature, low surface trap density, and flat device interface.

To further investigate photodetector performance, we performed detailed photoresponse measurements. Fig. 4a presents typical EQE and $R$ spectra of the device measured under 0 V bias conditions. Notably, the device exhibits high EQEs (>40%) over a wide wavelength range from 350–840 nm, reaching a desirable peak value of 82.5% in the NIR region (750–840 nm). Correspondingly, the $R$ value reached ~0.53 A $W^{-1}$ at 800 nm, which is considerably higher than that of a commercial silicon-based device (Hamamatsu S1133-14, of less than 0.35 A $W^{-1}$).[46] The noise current ($i_n$) is usually directly related to the detection capability of photodetectors to monitor weak signals. Usually, the noise current comprises thermal noise, shot noise, and flicker noise.[12] From the noise power density of the Sn–Pb mixed single-crystal photodetector (Fig. 4b), we found that the low-frequency noise (i.e. $1/f$) dominates the noise current, and the noise current of the device under 0 V bias is as low as $3.9 \times 10^{-27}$ $A^2$ $Hz^{-1}$ at 1 Hz. Based on the measured noise current ($i_n$) and $R$, the specific detectivity ($D^*$) can be calculated according to the following expressions:[47]
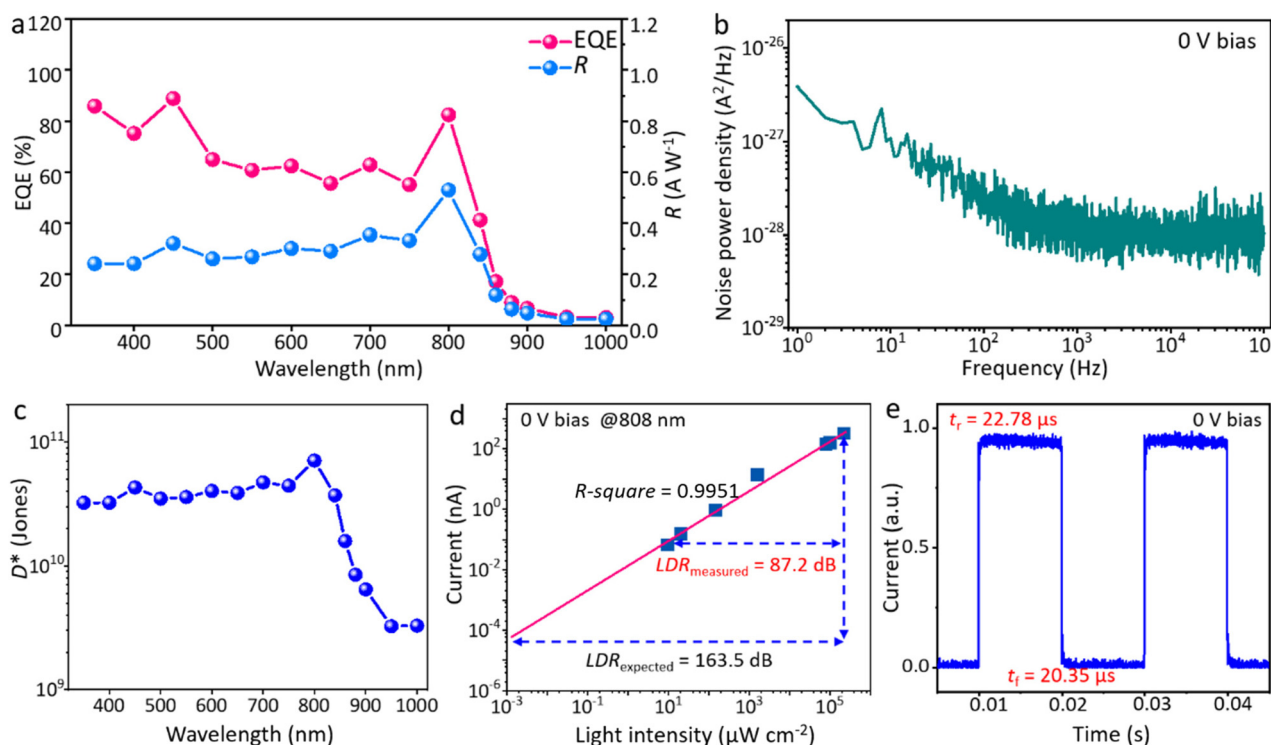
$$D^* = \frac{\sqrt{ABR}}{i_n}$$



**Fig. 4** (a) EQE and $R$ of the perovskite single-crystal NIR photodetector under 0 V bias. (b) Noise power density of the device under 0 V bias. (c) $D^*$ of the photodetector at various light wavelengths under 0 V bias. (d) The LDR of the NIR photodetector under the illumination of 808 nm light under 0 V bias. (e) Phototransient response of the device under a light modulation frequency of 50 Hz.

where $A$ is the device area, $B$ is the frequency, and NEP ($i_n/R$) is the noise equivalent power. As shown in Fig. 4c, $D^*$ is above $1.59 \times 10^{10}$ cm $Hz^{1/2}$ $W^{-1}$ from 350 to 860 nm, with a peak value of $7.09 \times 10^{10}$ cm $Hz^{1/2}$ $W^{-1}$ in the NIR region. This value is comparable to that of solution-processed organic NIR photodiode and perovskite/organic bulk heterojunction photodetectors.[48,49]

The LDR is particularly important for practical photodetection applications, especially in image sensors, since they need to operate over a broad intensity range to extract the detected light intensity from the corresponding photocurrent.[27] The LDR is commonly expressed on a logarithmic scale as:

$$\text{LDR} = 20 \log \frac{L_{\max}}{L_{\min}}$$

where $L_{\max}$ and $L_{\min}$ are the upper and lower limits of the light intensity in the linear photoresponse range, respectively. Fig. 4d and Fig. S7, ESI† show the current of photodetectors illuminated by 808 nm NIR light with different intensities. It can be clearly observed that the photocurrent gradually increases for a dynamic light intensity ranging from 9.8 μW $cm^{-2}$ to 224.9 mW $cm^{-2}$, satisfying a linear relationship with

the coefficient of determination ($R$-square) of up to 0.9951. The result corresponds to an LDR value of 87.2 dB. Given that the lower limit of LDR is restricted by the light intensity of the source, we calculated the expected LDR value to be 163.5 dB based on the illumination intensity (1.5 nW $cm^{-2}$) corresponding to the noise current, which is largely superior to that of previously reported Sn–Pb polycrystalline film-based NIR photodetectors (Table S2, ESI†).[14,18,20,22] Such a large linear response may result from the excellent carrier transport property and low trap density in the $(FASnI_3)_{0.1}(MAPbI_3)_{0.9}$ single crystal. Finally, the response speed of this perovskite single-crystal NIR photodetector was evaluated by measuring the transient photocurrent. In this measurement, the device was under chopper-modulated 808 nm LED illumination at a frequency of 50 Hz, and the transient photocurrent signal was recorded. The rise time and fall time are defined as the time required for the transient photocurrent varying from 10% to 90% and from 90% to 10% of the maximum value.[50] Under 0 V bias, the self-powered $(FASnI_3)_{0.1}(MAPbI_3)_{0.9}$ single-crystal photodetector achieved a rise time of 22.78 μs and a fall time of 20.35 μs, which can meet the requirements of many application scenarios. Stability is a major issue for the Sn–Pb mixed
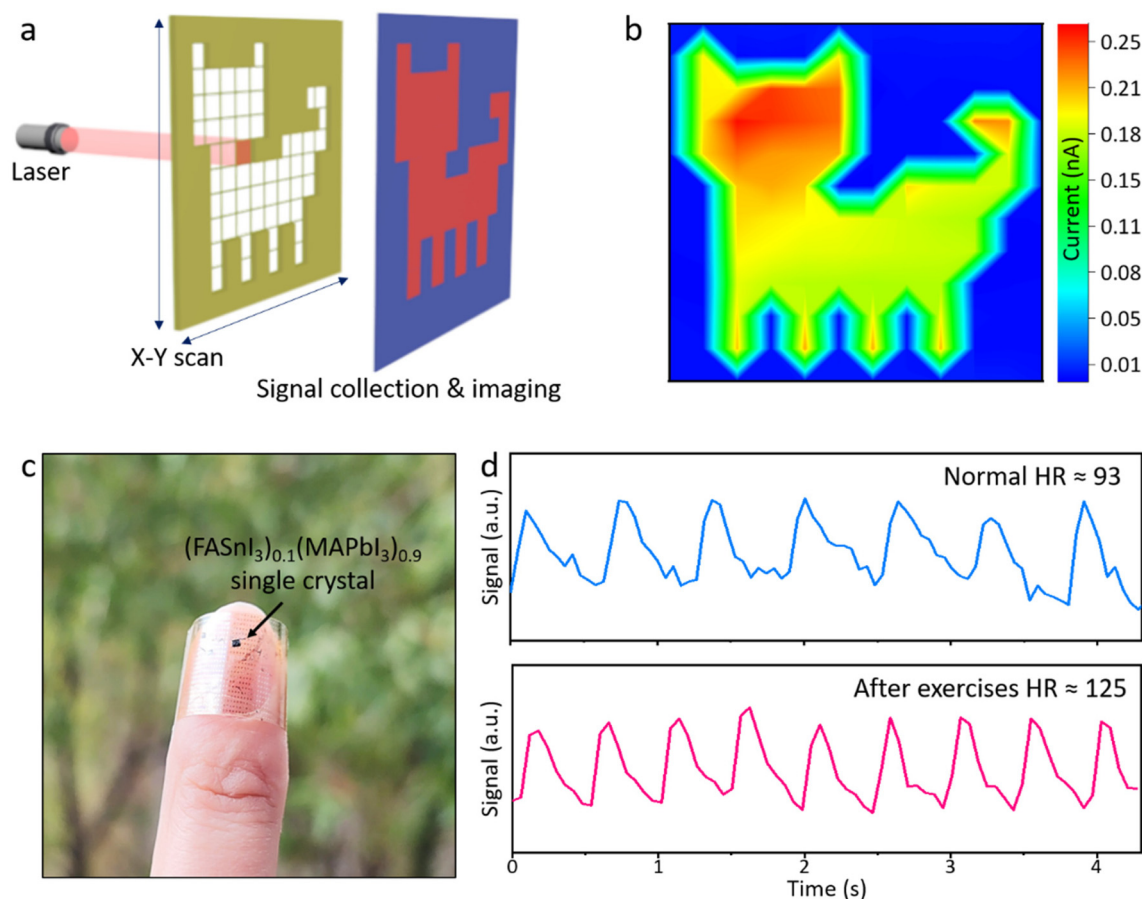


**Fig. 5** (a) Schematic of the image scanning system for the $(FASnI_3)_{0.1}(MAPbI_3)_{0.9}$ single crystal-based NIR photodetector. (b) NIR imaging result. (c) A photo of the perovskite single-crystal photodetector on the flexible substrate. (d) Pulse signals obtained from the flexible perovskite single crystal NIR photodetector under normal (upper) and after-exercise (lower) conditions.

perovskite-based photodetector. Here, we monitored the changes in the photocurrent and dark current of the non-encapsulated devices (Fig. S8, ESI†). It is clearly seen that there is almost no discernible degradation in the photocurrent and dark current. The good air stability is because the grain boundary-free perovskite single crystal prevents water and oxygen destruction, which dramatically improves the stability of $Sn^{2+}$ in the atmospheric environment.[26,27]

The $(FASnI_3)_{0.1}(MAPbI_3)_{0.9}$ single-crystal photodetector with excellent comprehensive performance provides great prospects for NIR imaging applications. To demonstrate this, the $(FASnI_3)_{0.1}(MAPbI_3)_{0.9}$ single-crystal photodetector scanned the imaging target of a "cat" in two dimensions, and the current was recorded during scanning, as shown in Fig. 5a. After that, the output current values were used to reconstruct the target image. Fig. 5b shows the NIR imaging result of the target image, and the profile of the cat can be clearly captured, highlighting the NIR recognition imaging ability of the $(FASnI_3)_{0.1}(MAPbI_3)_{0.9}$ single-crystal photodetector. Moreover, the high-sensitivity and self-powered NIR photodetector is very favorable for wearable real-time health monitoring applications, such as a photoplethysmogram (PPG). The PPG sensor uses a photodetector to measure the change in the intensity of the NIR light that passes through the blood vessels.[3] In this work, we fabricated the $(FASnI_3)_{0.1}(MAPbI_3)_{0.9}$ single-crystal NIR photodetector on a flexible substrate to monitor the intensity change of light that passes through a fingertip (Fig. 5c). The output current signals of one of the authors under their resting and after-exercise conditions were recorded, as shown in Fig. 5d. The typical systolic and diastolic peaks in the output signals can be identified clearly. By implementing the fast Fourier transform (FFT) (Fig. S9, ESI†), the heart rate (HR) of the author under resting and after-exercise conditions was determined to be 93 and 125 beats min$^{-1}$, respectively. More importantly, our self-driven $(FASnI_3)_{0.1}(MAPbI_3)_{0.9}$ single-crystal NIR photodetector could produce very stable PPG signals with large signal noise ratios of 18.1 and 24.9 dB under resting and after-exercise conditions.

## Conclusion

In summary, we reported a low-temperature space-confined technique to grow narrow-bandgap Sn–Pb mixed perovskite single crystals for high-performance NIR photodetectors. The key is to introduce a confined space at room temperature to decrease the crystallization rate, which avoids phase separation, enabling the realization of pure-phase Sn–Pb mixed perovskite single crystals. With this method, high-mobility and low-trap $(FASnI_3)_{0.1}(MAPbI_3)_{0.9}$ single crystals can be controllably prepared. Due to the high-quality $(FASnI_3)_{0.1}(MAPbI_3)_{0.9}$ single crystal, its self-driven NIR photodetector exhibits outstanding comprehensive performance in terms of a high EQE of 82.5%, large $R$ of 0.53 A W$^{-1}$, high $D^*$ of $7.09 \times 10^{10}$ Jones, broad LDR of up to 163.5 dB, and fast response speed in the NIR spectral region (750–860 nm). NIR imaging and self-powered HR monitoring were successfully demonstrated with the optimized $(FASnI_3)_{0.1}(MAPbI_3)_{0.9}$ single-crystal photodetector, indicating the potential of Sn–Pb mixed perovskite single crystals for practical implementation as highly efficient photodetection platforms.

## Author contributions

W. D, X. Z. and J. S. proposed the idea, designed the experiments and wrote the manuscript. Z. C. and Z. L. performed the experiments and device measurements. Y. S. performed the optical measurement and optimized the scheme and figures. Z. C. and Z. L. contributed equally to this work.

## Conflicts of interest

There are no conflicts to declare.

## Acknowledgements

## References

1 T. Yokota, T. Nakamura, H. Kato, M. Mochizuki, M. Tada, M. Uchida, S. Lee, M. Koizumi, W. Yukita, A. Takimoto and T. Someya, *Nat. Electron.*, 2020, **3**, 113–121.

2 F. Cao, J. Chen, D. Yu, S. Wang, X. Xu, J. Liu, Z. Han, B. Huang, Y. Gu, K. L. Choy and H. Zeng, *Adv. Mater.*, 2020, **32**, 1905362.

3 H. J. Eun, H. Lee, Y. Shim, G. U. Seo, A. Y. Lee, J. J. Park, J. Heo, S. Park and J. H. Kim, *iScience*, 2022, **25**, 104194.

4 L. J. Pi, P. F. Wang, S. J. Liang, P. Luo, H. Y. Wang, D. Y. Li, Z. X. Li, P. Chen, X. Zhou, F. Miao and T. Y. Zhai, *Nat. Electron.*, 2022, **5**, 248–254.

5 C. Liu, J. Guo, L. Yu, J. Li, M. Zhang, H. Li, Y. Shi and D. Dai, *Light: Sci. Appl.*, 2021, **10**, 123.

6 R. M. Saadabad, A. Olk, D. N. Neshev and A. E. Miroshnichenko, *IEEE*, 2021, **10**, 123.

7 H. Zhang, W. Wang, S. Yip, D. Li, F. Li, C. Lan, F. Wang, C. Liu and J. C. Ho, *J. Mater. Chem. C*, 2020, **8**, 17025.

8 Y. Pinki, S. Dewan, R. Mishra and S. Das, *J. Phys. D: Appl. Phys.*, 2022, **55**, 313001.

9 J. M. Choi, H. Y. Jang, A. R. Kim, J. D. Kwon, B. Cho, M. H. Park and Y. Kim, *Nanoscale*, 2021, **13**, 672.

10  Z. Zhao, C. Xu, Y. Ma, X. Ma, X. Zhu, L. Niu, L. Shen, Z. Zhou and F. J. Zhang, *Adv. Funct. Mater.*, 2022, **32**, 2212149.

11  K. Yang, Z. Zhao, M. Liu, L. Niu, X. Zhao, G. Yuan, X. Ma and F. J. Zhang, *J. Mater. Chem. C*, 2022, **10**, 10888–10894.

12  M. Liu, J. Wang, K. Yang, Z. Zhao, Z. Zhou, Y. Ma, L. Shen, X. Ma and F. J. Zhang, *J. Mater. Chem. C*, 2021, **9**, 6357–6364.

13  X. Ruan, S. Cheng, W. Deng, Y. Tan, Z. Lu, J. Shi, X. Zhang and J. Jie, *Adv. Electron. Mater.*, 2022, **8**, 2200355.

14  H. L. Zhu, Z. Liang, Z. Huo, W. K. Ng, J. Mao, K. S. Wong, W.-J. Yin and W. C. H. Choy, *Adv. Funct. Mater.*, 2018, **28**, 1706068.

15  S. Gielen, C. Kaiser, F. Verstraeten, J. Kublitski, J. Benduhn, D. Spoltore, P. Verstappen, W. Maes, P. Meredith, A. Armin and K. Vandewal, *Adv. Mater.*, 2020, **32**, 2003818.

16  L. Pi, P. Wang, S. J. Liang, P. Luo, H. Wang, D. Li, Z. Li, P. Chen, X. Zhou, F. Miao and T. Zhai, *Nat. Electron.*, 2022, **5**, 248–250.

17  W. Deng, Y. Lv, X. Ruan, X. Zhang, R. Jia, Y. Yu, Z. Liu, D. Wu, X. Zhang and J. Jie, *Laser Photonics Rev.*, 2022, **16**, 2022283.

18  W. Wang, D. Zhao, F. Zhang, L. Li, M. Du, C. Wang, Y. Yu, Q. Huang, M. Zhang, L. Li, J. Miao, Z. Lou, G. Shen, Y. Fang and Y. Yan, *Adv. Funct. Mater.*, 2017, **27**, 1703953.

19  X. Xu, C. C. Chueh, P. Jing, Z. Yang, X. Shi, T. Zhao, L. Y. Lin and A. K. Y. Jen, *Adv. Funct. Mater.*, 2017, **27**, 1701053.

20  Y. Zhao, C. Li, J. Jiang, B. Wang and L. Shen, *Small*, 2020, **16**, 2001534.

21  Z. Han, W. Fu, Y. Zou, Y. Gu, J. Liu, B. Huang, D. Yu, F. Cao, X. Li, X. Xu and H. Zeng, *Adv. Mater.*, 2021, **33**, 2003852.

22  N. Ma, J. Jiang, Y. Zhao, L. He, Y. Ma, H. Wang, L. Zhang, C. Shan, L. Shen and W. Hu, *Nano Energy*, 2021, **86**, 106113.

23  H. L. Zhu, H. Lin, Z. Song, Z. Wang, F. Ye, H. Zhang, W. J. Yin, Y. Yan and W. C. H. Choy, *ACS Nano*, 2019, **13**, 11800.

24  H. Liu, H. L. Zhu, Z. Wang, X. Wu, Z. Huang, M. R. Huqe, J. A. Zapien, X. Lu and W. C. H. Choy, *Adv. Funct. Mater.*, 2021, **31**, 2010532.

25  R. Ding, C. K. Liu, Z. Wu, F. Guo, S. Y. Pang, L. W. Wong, W. F. Io, S. Yuan, M. C. Wong, M. B. Jedrzejczyk, J. Zhao, F. Yan and J. Hao, *Nano Lett.*, 2020, **20**, 2747.

26  W. Deng, J. Jie, X. Xu, Y. Xiao, B. Lu, X. Zhang and X. Zhang, *Adv. Mater.*, 2020, **32**, 1908340.

27  Q. Chen, J. Luo, R. He, H. Lai, S. Ren, Y. Jiang, Z. Wan, W. Wang, X. Hao, Y. Wang, J. Zhang, I. Constantinou, C. Wang, L. Wu, F. Fu and D. Zhao, *Adv. Energy Mater.*, 2021, **11**, 2102045.

28  C. Li, Y. Pan, J. Hu, S. Qiu, C. Zhang, Y. Yang, S. Chen, X. Liu, C. J. Brabec, M. K. Nazeeruddin, Y. Mai and F. Guo, *ACS Energy Lett.*, 2020, **5**, 1386.

29  W. G. Choi, S. Na, C. G. Park and T. Moon, *Sol. Energy*, 2019, **178**, 56–60.

30  L. A. Muscarella, D. Petrova, R. Jorge Cervasio, A. Farawar, O. Lugier, C. McLure, M. J. Slaman, J. Wang, B. Ehrler, E. von Hauff and R. M. Williams, *ACS Appl. Mater. Interfaces*, 2019, **11**, 17555.

31  B. Slimi, M. Mollar, I. B. Assaker, I. Kriaa, R. Chtourou and B. Marí, *Energy Procedia*, 2016, **102**, 87–95.

32  Z. Chen, Q. Dong, Y. Liu, C. Bao, Y. Fang, Y. Lin, S. Tang, Q. Wang, X. Xiao, Y. Bai, Y. Deng and J. Huang, *Nat. Commun.*, 2017, **8**, 1890.

33  Y. Song, W. Bi, A. Wang, X. Liu, Y. Kang and Q. Dong, *Nat. Commun.*, 2020, **11**, 274.

34  W. Pan, H. Wu, J. Luo, Z. Deng, C. Ge, C. Chen, X. Jiang, W. Yin, G. Niu, L. Zhu, L. Yin, Y. Zhou, Q. Xie, X. Ke, M. Sui and J. Tang, *Nat. Photonics*, 2017, **11**, 726–732.

35  A. A. Zhumekenov, V. M. Burlakov, M. I. Saidaminov, A. Alofi, M. A. Haque, B. Turedi, B. Davaasuren, I. Dursun, N. Cho, A. M. El-Zohry, M. D. Bastiani, A. Giugni, B. Torre, E. D. Fabrizio, O. F. Mohammed, A. Rothenberger, T. Wu, A. Goriely and O. M. Bakr, *ACS Energy Lett.*, 2017, **2**, 1782–1788.

36  Y. Liu, Y. Zhang, Z. Yang, H. Ye, J. Feng, Z. Xu, X. Zhang, R. Munir, J. Liu, P. Zuo, Q. Li, M. Hu, L. Meng, K. Wang, D. M. Smilgies, G. Zhao, H. Xu, Z. Yang, A. Amassian, J. Li, K. Zhao and S. F. Liu, *Nat. Commun.*, 2018, **9**, 5302.

37  Z. Yang, Q. Xu, X. Wang, J. Lu, H. Wang, F. Li, L. Zhang, G. Hu and C. Pan, *Adv. Mater.*, 2018, **30**, 1802110.

38  Y. Liu, Y. Zhang, K. Zhao, Z. Yang, J. Feng, X. Zhang, K. Wang, L. Meng, H. Ye, M. Liu and S. F. Liu, *Adv. Mater.*, 2018, **30**, 1707314.

39  Y. C. Liu, Y. X. Zhang, Z. Yang, J. S. Feng, Z. Xu, Q. X. Li, M. X. Hu, H. C. Ye, X. Zhang, M. Liu, K. Zhao and S. Z. Liu, *Mater. Today*, 2019, **22**, 67–75.

40  Y. Liu, Q. Dong, Y. Fang, Y. Lin, Y. Deng and J. Huang, *Adv. Funct. Mater.*, 2019, **29**, 1807707.

41  Z. Cheng, K. Liu, J. Yang, X. Chen, X. Xie, B. Li, Z. Zhang, L. Liu, C. Shan and D. Shen, *ACS Appl. Mater. Interfaces*, 2019, **11**, 34144.

42  F. Yao, J. Peng, R. Li, W. Li, P. Gui, B. Li, C. Liu, C. Tao, Q. Lin and G. Fang, *Nat. Commun.*, 2020, **11**, 1194.

43  Y. Chen, Y. Lei, Y. Li, Y. Yu, J. Cai, M. H. Chiu, R. Rao, Y. Gu, C. Wang, W. Choi, H. Hu, C. Wang, Y. Li, J. Song, J. Zhang, B. Qi, M. Lin, Z. Zhang, A. E. Islam, B. Maruyama, S. Dayeh, L.-J. Li, K. Yang, Y. H. Lo and S. Xu, *Nature*, 2020, **577**, 209–215.

44  Y. Zhou, K. Fernando, J. Wan, F. Liu, S. Shrestha, J. Tisdale, C. J. Sheehan, A. C. Jones, S. Tretiak, H. Tsai, H. Huang and W. Nie, *Adv. Funct. Mater.*, 2021, **31**, 2101058.

45  H. Hu, S. Moghadamzadeh, R. Azmi, Y. Li, M. Kaiser, J. C. Fischer, Q. Jin, J. Maibach, I. M. Hossain, U. W. Paetzold and B. A. Nejand, *Adv. Funct. Mater.*, 2022, **32**, 2107650.

46  C. F. Fuentes-Hernandez, W. F. Chou, T. M. Khan, L. Diniz, J. Lukens, F. A. Larrain, V. A. Rodriguez-Toro and B. Kippelen, *Science*, 2020, **370**, 698–701.

47 W. Deng, J. Jie, Q. Shang, J. Wang, X. Zhang, S. Yao, Q. Zhang and X. Zhang, *ACS Appl. Mater. Interfaces*, 2015, **7**, 2039–2045.

48 J. Huang, J. Lee, J. Vollbrecht, V. V. Brus, A. L. Dixon, D. X. Cao, Z. Zhu, Z. Du, H. Wang, K. Cho, G. C. Bazan and T. Q. Nguyen, *Adv. Mater.*, 2020, **32**, 1906027.

49 C. Li, H. Wang, F. Wang, T. Li, M. Xu, H. Wang, Z. Wang, X. Zhan, W. Hu and L. Shen, *Light: Sci. Appl.*, 2020, **9**, 31.

50 Z. Zhao, M. Liu, K. Yang, C. Xu, Y. Guan, X. Ma, J. Wang and F. J. Zhang, *Adv. Funct. Mater.*, 2021, **31**, 2106009.

This journal is © The Royal Society of Chemistry 2023